Dynamic patterns in a two-dimensional neural field with refractoriness

Yang Qi and Pulin Gong
School of Physics, University of Sydney, New South Wales 2006, Australia
(Received 30 March 2015; published 10 August 2015)

The formation of dynamic patterns such as localized propagating waves is a fascinating self-organizing phenomenon that happens in a wide range of spatially extended systems including neural systems, in which they might play important functional roles. Here we derive a type of two-dimensional neural-field model with refractoriness to study the formation mechanism of localized waves. After comparing this model with existing neural-field models, we show that it is able to generate a variety of localized patterns, including stationary bumps, localized waves rotating along a circular path, and localized waves with longer-range propagation. We construct explicit bump solutions for the two-dimensional neural field and conduct a linear stability analysis on how a stationary bump transitions to a propagating wave under different spatial eigenmode perturbations. The neural-field model is then partially solved in a comoving frame to obtain localized wave solutions, whose spatial profiles are in good agreement with those obtained from simulations. We demonstrate that when there are multiple such propagating waves, they exhibit rich propagation dynamics, including propagation along periodically oscillating and irregular trajectories; these propagation dynamics are quantitatively characterized. In addition, we show that these waves can have repulsive or merging collisions, depending on their collision angles and the refractoriness parameter. Due to its analytical tractability, the two-dimensional neural-field model provides a modeling framework for studying localized propagating waves and their interactions.

DOI: 10.1103/PhysRevE.92.022702 PACS number(s): 87.19.ll, 87.19.lq

I. INTRODUCTION

Localized propagating waves with a variety of names, such as dissipative solitons, dissipative breathers, traveling spots, and pulses, have been found in systems ranging from chemical and physical reaction-diffusion systems [1–6] to biological cells [7–9] and neural systems [10,11]. Understanding their formation mechanisms and complex dynamics is a new frontier in the study of spatiotemporal patterns of these diverse systems. In neural systems, the dynamics of such waves may play an essential role in cortical information processing; recently, it has been suggested that these waves and their interactions can be used to implement distributed dynamic computation: Information might be encoded in these waves, information might be communicated based on their propagation, and information might be processed when these waves interact or collide with each other [12].

To study the formation of localized propagating waves, a simple two-dimensional, spiking neural network model is developed in [13], in which each neuron has three states, i.e., the resting, the firing, and the refractory states. In the model, each neuron in the resting state can be excited by an above-threshold input; it then becomes refractory, after which it returns to the resting state and can be excited again. Such excitable dynamics capture the typical firing behavior of neurons and similar activity in other excitable systems as well [14–18]. The model explicitly takes the refractoriness of neural firing activity into consideration. Refractoriness, just like the spiking of neurons, is a fundamental part of neural activity, which results from the intrinsic dynamics of the active membrane conductance responsible for spike generation [19,20]. During this refractory period, neurons that have just fired are unable to produce another spike regardless of the strength of afferent stimuli [20]. For this reason, one might think that refractoriness would limit the performance of neurons. However, it has been shown that refractoriness plays an essential role in increasing the response reliability and precision of firing activity of individual neurons and in increasing their information transfer rates [21]. Theoretical modeling studies on individual neurons have shown that, by including refractoriness in widely used rate-based neural models using Poisson processes, the models better capture the statistical properties of spike trains of individual neurons than using Poisson processes alone [22–24] and that refractoriness can result in periodic neural oscillations [25]. Modeling studies on spatially extended neural systems with refractoriness have shown the existence of self-organized spatiotemporal patterns, particularly spiral waves [26,27], similar to those found in other spatially extended excitable media with refractoriness [28,29]. In a two-dimensional spiking neural circuit model developed recently [13], it has been shown that refractoriness plays an essential role in the formation of localized propagating waves; a similar effect of refractoriness in a one-dimensional continuous neural-field model has been analyzed in [30].

In this study, we apply a mean-field treatment to the two-dimensional spiking neural network model in [13] to derive a new type of two-dimensional neural field. We then show the differences between this model and the existing neural-field models. Due to its analytical tractability, it provides insights into understanding the formation of localized propagating waves and their dynamics in two-dimensional space. Neural fields with two spatial dimensions have a far richer repertoire of spatiotemporal patterns than those with only one dimension, but relatively fewer studies have focused on the former [31,32]. We show that, by varying a refractory parameter, our two-dimensional neural field can produce stationary bumps, crescent-shaped propagating waves with complex collective dynamics, and localized rotating waves near the transition between these bumps and waves. We construct explicit bump solutions for the two-dimensional neural field and conduct a linear stability analysis to show how symmetry breaking occurs under different spatial eigenmode

perturbations; in this analysis, a special treatment involving two auxiliary fields is applied to deal with the simultaneous presence of multiplicative nonlinearity and discontinuity at the bump boundary. We also investigate the complex dynamics of multiple localized waves and their interactions emerging from the neural field.

II. FROM SPIKING NETWORK TO CONTINUOUS NEURAL FIELD WITH REFRACTORINESS

In the three-state, spiking neural network model [13], the states of individual neurons change at discrete time steps as follows: (i) A neuron in the resting state remains at rest unless the total input it receives from other neurons is greater than a threshold value $\kappa = 1$, in which case it fires at the next time step. (ii) When a neuron is in the firing state, it sends outputs to other neurons to which it is connected and becomes refractory at the next time step. (iii) When a neuron is in the refractory state, it returns to the resting state with a constant probability p, otherwise remaining unchanged. We consider a two-dimensional network, where an ith neuron is located on a square lattice with coordinates (x_i, y_i). The state of the neuron at time step n is denoted by s_i^n, which takes a value of 1 for firing state, 0 for resting state, and -1 for refractory state. The full dynamics of the neural network can be described as

$$s_i^n = \begin{cases} H[I_i^{n-1} - \kappa], & \text{if} \quad s_i^{n-1} = 0, \\ -1, & \text{if} \quad s_i^{n-1} = 1, \\ 0 \text{ with probability } p, \text{ otherwise } -1, & \text{if} \quad s_i^{n-1} = -1, \end{cases} \tag{1}$$

where $H(x)$ is the Heaviside step function with $H(x) = 1$ if $x \geqslant 0$ and $H(x) = 0$ otherwise. The total synaptic input I_i^n received by the neuron is

$$I_i^n = \sum_j w_{ij} S_j^n, \tag{2}$$

where w_{ij} is a synaptic coupling function and $S_j^n = H(s_j^n - 1)$ represents the spike train of the neuron.

We now derive a continuous neural-field model based on this spiking neural network model. First, define the probability of the ith neuron being in firing, ready, and refractory state at a discrete time n as f_i^n, g_i^n, and h_i^n, respectively. A normalization condition requires that $f_i^n + g_i^n + h_i^n = 1$. Based on the transition rules of Eq. (1), the evolution of these probabilities over successive time steps can be described as follows:

$$\begin{cases} f_i^n = q_i^{n-1} g_i^{n-1}, \\ g_i^n = \left(1 - q_i^{n-1}\right) g_i^{n-1} + p h_i^{n-1}, \\ h_i^n = (1-p) h_i^{n-1} + f_i^{n-1}. \end{cases} \tag{3}$$

The transition from the refractory state to the resting state is determined by a constant probability $p \in [0,1]$, whereas the transition from resting state to firing state is determined by the probability that the total input I_i^n received by the neuron exceeds a threshold $\kappa = 1$, i.e., $q_i^n = P(I_i^n > \kappa)$. The spike train S_j^n is a random variable with a discrete probability distribution $P(S_j^n = 1) = f_j^n$ and $P(S_j^n = 0) = 1 - f_j^n$. In the spirit of central limit theorem (CLT), the probability distribution of the synaptic input I_i^n, as given by Eq. (2), can be approximated by a Gaussian distribution with a mean of

$$u_i^n = \sum_j w_{ij} \langle S_j^n \rangle = \sum_j w_{ij} f_j^n \tag{4}$$

and a variance of

$$\left[\sigma_i^n\right]^2 = \sum_{j,k} w_{ij} w_{ik} \mathrm{Cov}\left(f_j^n, f_k^n\right). \tag{5}$$

Given the probability distribution of I_i^n, the transition probability from the resting state to the firing state $q_i^n = P(I_i^n > \kappa)$ is

$$q_i^n \approx 1 - \Phi\left(\frac{\kappa - u_i^n}{\sigma_i^n}\right) = \Phi\left(\frac{u_i^n - \kappa}{\sigma_i^n}\right), \tag{6}$$

where $\Phi(x)$ denotes the cumulative distribution of the standard Gaussian. To further simplify the equations, we approximate the variance in Eq. (5) with a constant σ^2 for all neurons. This allows us to approximate q_i^n in Eq. (6) using a transfer function depending solely on u_i^n,

$$q_i^n = \phi\left(u_i^n\right). \tag{7}$$

For analytical tractability, a sigmoid transfer function is often used to approximate the cumulative Gaussian distribution. In the limit as $\sigma \to 0$, the transfer function approaches a Heaviside step function, $\phi(u_i^n) = H[u_i^n - \kappa]$, which is used in this study. This enables us to construct explicit solutions of localized bumps and to analytically determine their stability.

The next step is to replace the discrete lattice and the discrete time with a continuum of spatial position $\mathbf{r} \in \mathbb{R}^2$ and time $t \in \mathbb{R}$. The probabilities f_i^n, g_i^n, and h_i^n are then replaced by the following field variables, $f(\mathbf{r},t)$, $g(\mathbf{r},t)$, and $h(\mathbf{r},t)$, representing the fraction of firing, resting, and refractory neurons, respectively. The mean synaptic input [Eq. (4)] is therefore $u(\mathbf{r},t) = \int_{\mathbb{R}^2} w(\mathbf{r},\mathbf{r}') f(\mathbf{r}',t) d\mathbf{r}'$. In particular, for a distance-dependent coupling function, we have $w(\mathbf{r},\mathbf{r}') = w(|\mathbf{r} - \mathbf{r}'|)$, and the synaptic input is then a spatial convolution (denoted by "*"),

$$u(\mathbf{r},t) = w * f = \int_{\mathbb{R}^2} w(|\mathbf{r} - \mathbf{r}'|) f(\mathbf{r}',t) d\mathbf{r}'. \tag{8}$$

We also replace the finite difference in time with a corresponding derivative,

$$f(\mathbf{r},t) - f(\mathbf{r},t - \Delta t) \approx \tau \frac{\partial f(\mathbf{r},t)}{\partial t}, \tag{9}$$

and similarly for $g(\mathbf{r},t)$ and $h(\mathbf{r},t)$. The time constant is set to be $\tau = 10$ ms, typical for cortical neurons. For convenience during the subsequent mathematical analyses, we rescale the time using $t \leftarrow \tau t$. By applying Eq. (9) to Eq. (3), we obtain a set of continuous equations as a mean-field approximation to the original spiking network,

$$\begin{cases} \partial_t f = -f + g H(u - \kappa), \\ \partial_t g = -g H(u - \kappa) + p h, \\ \partial_t h = -p h + f. \end{cases} \tag{10}$$

By reinforcing the normalization condition $g = 1 - f - h$, the neural field is simplified into a pair of equations,

$$\begin{cases} \dfrac{\partial f}{\partial t} = -f + (1 - f - h)H(u - \kappa), \\ \dfrac{\partial h}{\partial t} = -ph + f, \end{cases} \tag{11}$$

where $u = w * f$, as defined in Eq. (8), and $\kappa = 1$ is the firing threshold.

In this study, we consider a lateral inhibitory coupling constructed from Bessel functions as in [33], due to its analytical tractability,

$$w(r) = W_E w_K(r/\sigma_E) - W_I w_K(r/\sigma_I), \tag{12}$$

where $w_K(r) = \frac{2}{3\pi}[K_0(r) - K_0(2r)]$ and K_ν is the modified Bessel function of the second kind. The subscripts E and I denote the excitatory and the inhibitory coupling, respectively. The function $w_K(r)$ approximates the exponential function $\frac{1}{2\pi}e^{-r}$, and it is normalized such that $\int_{\mathbb{R}^2} w_K(r)d\mathbf{r} = 1$. The overall strength of the coupling function is therefore $\int_{\mathbb{R}^2} w(r)d\mathbf{r} = W_E\sigma_E^2 - W_I\sigma_I^2$. Here we let $W_E = 144.4$, $W_I = 73.7$, $\sigma_E = 0.187$ mm, and $\sigma_I = 0.324$ mm, resulting in a Mexican hat coupling with short-range excitation and longer-range inhibition, whose shape matches approximately that in the original spiking network model [13]. As in [13], the spatial scales σ_E and σ_I are chosen such that the size of the localized waves generated by the neural field is similar to that of cortical waves found in experiments [10,34]. As described in Eq. (11), the two-dimensional neural field involves two sources of nonlinearity; one is the discontinuity posed by the Heaviside transfer function, and the other is the multiplier $(1 - f - h)$ representing the fraction of resting neurons. The terms f and h in this multiplier therefore act as nonlinear negative feedbacks in this neural-field model. In this study, we investigate the effect of refractoriness on the neural-field dynamics by varying p, the rate of transition from the refractory state to the resting state; note that the transition rate p is inversely proportional to the refractory period.

III. COMPARISON WITH OTHER NEURAL-FIELD MODELS

Before proceeding to analyzing the neural-field model, we first compare it with other neural-field models with negative feedback. The most studied neural field with negative feedback involves a linear recovery variable [35],

$$\begin{cases} \tau\partial_t f = -f - h + \phi(w * f), \\ \partial_t h = -\alpha h + \beta f. \end{cases} \tag{13}$$

This type of neural-field model can produce spatially localized patterns in both one and two spatial dimensions, including traveling pulses, stationary bumps, and breathers [31,33,36,37]. However, a more biologically plausible description of negative feedback should be nonlinear [38]. There has been a limited number of studies on neural fields with nonlinear negative feedback, which takes the form of synaptic depression [39–41], spike frequency adaptation [39,42,43], or refractoriness [25,30,38]. Even fewer studies have extended the analyses of these types of neural fields to the cases with two spatial dimensions [40,41]. In the following, we compare our model to those in [30,40,41].

A one-dimensional neural field with refractoriness is described as [30]

$$\begin{cases} \tau\partial_t f = -f + (1 - h)\phi(w * f), \\ h = \frac{1}{R}\int_{t-R}^{t} f(x,t')dt', \end{cases} \tag{14}$$

where the variable $h(x,t)$ represents the fraction of neurons in the refractory state and R is the absolute refractory period. The premultiplier $(1 - h)$ in Eq. (14) is therefore interpreted as the fraction of resting neurons. Linear Turing analysis and weakly nonlinear analysis are used to investigate the emergence of spatiotemporally periodic waves in this model [30]. There are three differences between our model and this model. First, the premultiplier representing the fraction of resting neurons is $(1 - h - f)$ in Eq. (11) of our model, instead of $(1 - h)$ in Eq. (14). This means that our model provides a more exact description for the fraction of resting neurons by explicitly excluding the fraction of currently firing neurons from it. Second, the dynamics of the refractory variable h in our model is described by an ordinary differential equation [second line of Eq. (11)], instead of the integral form in Eq. (14), equivalent to a delay differential equation. This significantly simplifies some steps in the subsequent mathematical analysis. Last, our neural field extends to two spatial dimensions, allowing the formation of complex spatiotemporal patterns that cannot be formed in one-dimensional models, as shown in later sections.

Another neural field to be compared with ours is a two-dimensional neural field with synaptic depression [40,41],

$$\begin{cases} \tau\partial_t f = -f + g\phi(w * f), \\ \partial_t g = -\beta g\phi(w * f) + (1 - g)/\alpha, \end{cases} \tag{15}$$

where the premultiplier $g(\mathbf{r},t)$ is the fraction of available presynaptic resources, which depletes at a rate of $\beta g\phi(u)$ and regenerates at a rate of $(1 - g)/\alpha$. It has been shown that the neural field forms an oscillatory medium due to the nonlinear feedback in the form of synaptic depression [40]. With a purely excitatory coupling, this neural field can generate an oscillating core that periodically emits radially expanding target waves, and perturbation to this oscillating core results in the formation of spiral waves.

At first glance, a neural field with synaptic depression [Eq. (15)] has an entirely different mathematical form as that with refractoriness [Eq. (14)]. However, the derivation of our model reveals an intriguing connection between them. To illustrate this, consider Eq. (10), the set of three equations used to derive Eq. (11) before imposing the normalization condition $f + g + h = 1$. If we choose to eliminate g from Eq. (10) by using $g = 1 - h - f$, we obtain a neural field with refractoriness [Eq. (11)]; if we choose to eliminate h using $h = 1 - g - f$ instead, we obtain a neural-field model,

$$\begin{cases} \partial_t f = -f + g\phi(w * f), \\ \partial_t g = -g\phi(w * f) + p(1 - f - g), \end{cases} \tag{16}$$

which is in a similar form as Eq. (15) with synaptic depression. This means that neural-field models with either refractoriness or synaptic depression are largely equivalent at a mathematical level. The key to establishing this connection is that a population of neurons is made up of all three fractions, f,

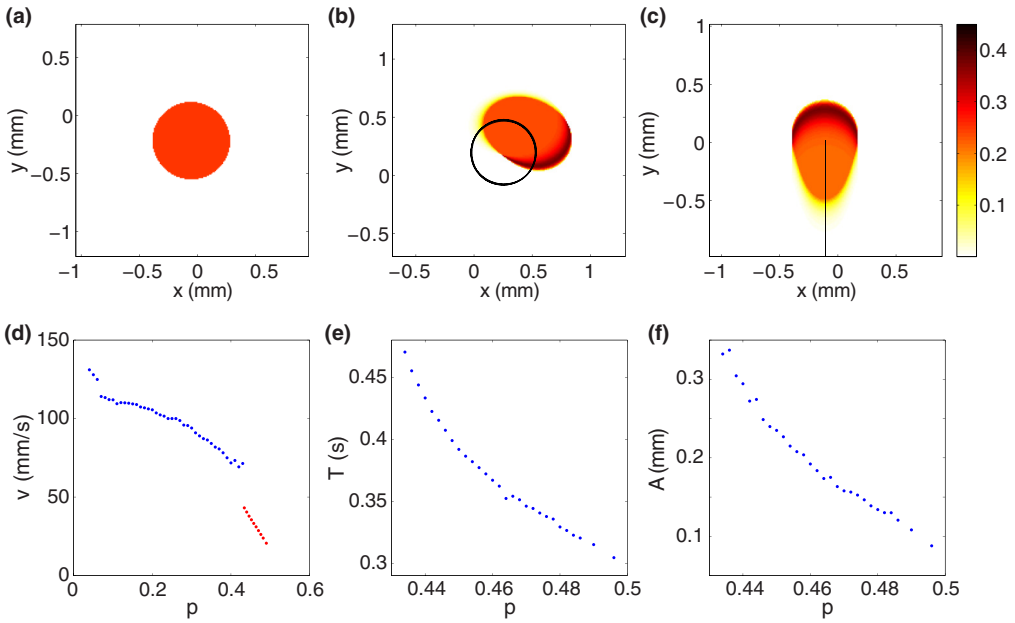

FIG. 1. (Color online) Spatially localized patterns of the neural field. (a) Snapshot of the firing rate $f(\mathbf{r},t)$ at $p = 0.5$, showing a stationary bump in the shape of a radially symmetric disk with radius $a = 0.33$ mm. (b) A rotating wave at $p = 0.44$ moving clockwise at a period of $T = 0.43$ s. The solid line shows its circular trajectory with a radius of $A = 0.29$ mm. (c) Snapshot of a crescent-shaped wave at $p = 0.38$ propagating upwards at a speed of $v = 78$ mm/s. The solid line traces the trajectory of the wave. (d) Speed of a propagating wave ($p < 0.43$) and tangential speed of a rotating wave ($p > 0.43$) versus p. (e) Period of a rotating wave versus p. (f) Radius of the trajectory of a rotating wave versus p.

g, and h, whereas in both [40] and [30], the fraction of firing neurons f is neglected. As a consequence, our model incorporates explicitly the fraction of firing neurons f as part of the nonlinear negative feedback, which, however, is missing in other models.

IV. REFRACTORINESS-INDUCED SYMMETRY BREAKING

Localized patterns including stationary bumps and localized propagating waves can emerge from the continuous neural field [Eq. (11)]. Figure 1(a) shows a stationary bump in the shape of a circular disk, which is formed in the parameter range $p > 0.49$; such a bump can be elicited by a spatially localized, transient external input, and it remains persistent after the input is removed. As p decreases and passes a critical point, $p_c \approx 0.49$, spontaneous symmetry breaking occurs, and the bump evolves to a crescent-shaped, localized propagating wave [Figs. 1(b) and 1(c)]. Interestingly, the trajectory of the localized wave (solid trace) is a straight line for $p \leqslant 0.43$ [Fig. 1(c)], but it converges to a circle for $0.43 < p \leqslant 0.49$ and persists indefinitely [Fig. 1(b)]. The direction of the circular motion can be either counterclockwise or clockwise, depending on the initial condition. Note that such a localized rotating wave traveling in a circular path is not identified in the original three-state spiking model due to the presence of noise [13], and similar rotating waves have been found in a stimulus-driven neural field with linear adaptation [33]. We then numerically calculate the speed of these localized propagating waves at different p values. As shown in Fig. 1(d), both the speed of a traveling wave ($p < 0.43$) and that of a rotating wave ($p > 0.43$) decreases as p increases. In particular, the speed of a rotating wave appears to depend linearly on p. The speed drops discontinuously at $p = 0.43$, as a traveling wave transitions to a rotating wave, and again at $p = 0.49$, as it transitions to a stationary bump. For the rotating wave, we also calculate the period of its rotation and the radius of its circular trajectory, which are both found to decrease as p increases [Figs. 1(e) and 1(f)].

We now construct explicit bump solutions to Eq. (11) and determine their linear stability with respect to different perturbations. For a stationary bump with radius a, the neural field satisfies $u(r) < \kappa$ for $r > a$ and $u(r) > \kappa$ for $r < a$. In this case, Eq. (11) can be reduced to spatially uncoupled linear equations; for $r > a$,

$$\begin{cases} \dfrac{\partial f}{\partial t} = -f, \\ \dfrac{\partial h}{\partial t} = -ph + f, \end{cases} \tag{17}$$

which has a fixed point at $(\bar{f},\bar{h}) = (0,0)$, corresponding to a stable node, and for $r < a$,

$$\begin{cases} \dfrac{\partial f}{\partial t} = -2f - h + 1, \\ \dfrac{\partial h}{\partial t} = -ph + f, \end{cases} \tag{18}$$

which has a fixed point at $(\bar{f},\bar{h}) = (\frac{p}{1+2p}, \frac{1}{1+2p})$, corresponding to a stable focus. Note that $\bar{f}$ is a monotonic increasing function of $p \in [0,1]$; when $p = 1$ the fraction of firing neurons is at maximum value, $\bar{f} = 1/3$, and when $p = 0$, all neurons remain in the refractory state.

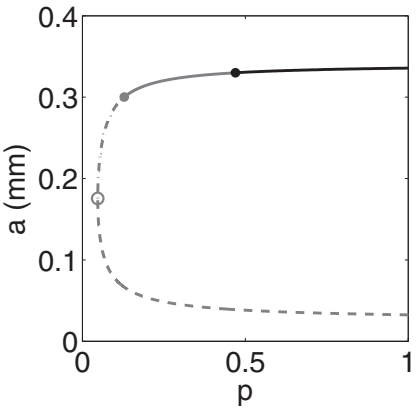

FIG. 2. The radius a of a bump solution at different p values. Two branches of bump solutions exist beyond a critical point $p \geqslant 0.047$ (circle). The lower branch (dashed line) is always unstable. For $p \leqslant 0.129$, the upper branch is stable with respect to a contraction and unstable to an expansion (dot-dashed line). For $0.129 < p < 0.470$, the upper branch is stable with respect to radially symmetric perturbations (expansion or contraction), but is unstable to a shift perturbation (solid gray line). For $p \geqslant 0.470$ the upper branch corresponds to stable stationary bumps (solid black line).

The neural-field model [Eq. (11)], therefore, has a steady-state solution in the form of a uniform disk, $\bar{f}(r) = \frac{p}{1+2p}$ and $\bar{h}(r) = \frac{1}{1+2p}$ for $r < a$, and $\bar{f}(r) = \bar{h}(r) = 0$ for $r > a$. The corresponding synaptic input is

$$\begin{aligned} \bar{u}(r) &= w * \bar{f} = \frac{p}{1+2p}\mathcal{I}(r), \\ \mathcal{I}(r) &= \int_0^{2\pi}\int_0^a w(|\mathbf{r}-\mathbf{r}'|)r'dr'd\theta'. \end{aligned} \tag{19}$$

By imposing the boundary condition $\bar{u}(a) = \kappa$, we obtain an existence condition for a radially symmetric bump,

$$p = \frac{\kappa}{\mathcal{I}(a) - 2\kappa}. \tag{20}$$

Note that for the coupling function used in the model [Eq. (12)], the integral $\mathcal{I}(a)$ can be expressed as a linear combination of Bessel functions [44],

$$\mathcal{I}(a) = \frac{4a}{3}[W_E\mathcal{I}_K(a,\sigma_E) - W_I\mathcal{I}_K(a,\sigma_I)], \tag{21}$$

where

$$\mathcal{I}_K(a,\sigma) = \sigma I_1(a/\sigma)K_0(a/\sigma) - \frac{\sigma}{2}I_1(2a/\sigma)K_0(2a/\sigma), \tag{22}$$

with I_ν denoting the modified Bessel function of the first kind of order ν. The dependence of the radius a of a stationary bump solution on the refractoriness parameter p, as described by Eq. (20), is shown in Fig. 2. For $p < 0.047$, no bump solution exists; at $p = 0.047$, a single bump solution exists with a radius of $a = 0.176$ mm; for each $p > 0.047$, there exists two bump solutions, one with a small radius and another with a large radius. Simulations show that the smaller bump is always unstable, whereas the larger bump is stable up until the critical point of symmetry breaking at $p_c = 0.49$. For neural fields with linear feedback, the stability is obtained by formally differentiating the Heaviside step function [33]. However, for neural fields with nonlinear feedback, this method fails to correctly identify the instabilities for symmetry breaking at p_c. This is because the eigenvalue for a perturbation near the bump boundary is different depending on the sign of the perturbation. The same kind of problem is found in a different neural-field model [41], where it is overcome by introducing an auxiliary field to the perturbation, whose sign can be explicitly described; by deriving an evolution equation for this auxiliary field and analyzing its linear stability, the stability of the bump in the original neural field can then be obtained [41].

Here we follow similar steps as in [41] to analyze our model, but with two modifications. First, the method in [41] is originally developed for analyzing a piecewise smooth system, but here we extend it to the case with piecewise continuity. Second, since our model has nonlinear feedback in both f and h, we introduce one more auxiliary field, in addition to the one used in [41]. Let $f(\mathbf{r},t) = \bar{f}(\mathbf{r}) + \epsilon\varphi(\mathbf{r},t)$ and $h(\mathbf{r},t) = \bar{h}(\mathbf{r}) + \epsilon\psi(\mathbf{r},t)$, where $\varphi(\mathbf{r},t)$ and $\psi(\mathbf{r},t)$ are small perturbations to the bump solutions. We also let $u = \bar{u} + \epsilon\mu$, where $\bar{u} = w * \bar{f}$ and $\mu = w * \varphi$. Substituting these into Eq. (11), we obtain,

$$\begin{cases} \partial_t\varphi = -\varphi - (\psi+\varphi)H(\bar{u}+\epsilon\mu-\kappa) \\ \qquad\quad + \dfrac{1}{\epsilon}(1-\bar{h}-\bar{f})H(\bar{u}+\epsilon\mu-\kappa) - \dfrac{1}{\epsilon}\bar{f}, & (23) \\ \partial_t\psi = -p\psi + \varphi. & (24) \end{cases}$$

The boundary condition after the perturbation satisfies

$$u(a+\epsilon\Delta,\theta,t) = \kappa, \tag{25}$$

where $\Delta(\theta,t)$ is the perturbation to the bump boundary. By expanding the above equation up to the first order in ϵ, we have

$$\kappa = u(a) + \epsilon\Delta u'(a) \approx \bar{u}(a) + \epsilon\mu(a) + \epsilon\Delta\bar{u}'(a) \tag{26}$$

and use $\bar{u}(a) = \kappa$ to get

$$\Delta(\theta,t) = \frac{\mu(a,\theta,t)}{|\bar{u}'(a)|}. \tag{27}$$

Note that we have not expanded the Heaviside step function in Eq. (23) due to the discontinuity of the premultiplier $1-\bar{h}-\bar{f}$ at the bump boundary. To proceed with the analysis of bump stability, we define the following pair of auxiliary fields:

$$\begin{cases} \Phi(\mathbf{r},t;\Delta) = \displaystyle\int_0^{2\pi}\int_0^{a+\epsilon\Delta(\theta',t)} w(|\mathbf{r}-\mathbf{r}'|)\varphi(\mathbf{r}',t)r'dr'd\theta', & (28) \\ \Psi(\mathbf{r},t;\Delta) = \displaystyle\int_0^{2\pi}\int_0^{a+\epsilon\Delta(\theta',t)} w(|\mathbf{r}-\mathbf{r}'|)\psi(\mathbf{r}',t)r'dr'd\theta'. & (29) \end{cases}$$

The variables Φ and Ψ incorporate explicitly the dependence on the sign of the perturbation near the bump boundary, allowing us to correctly determine the stability of the original perturbations φ and ψ by analyzing the stability of Φ and Ψ instead. Applying a spatial convolution to Eq. (23) with respect

to w and then substituting Eq. (28) into the result, we obtain

$$\partial_t \mu = -\mu - \Phi - \Psi + \frac{1}{\epsilon}\int_0^{2\pi}\int_0^{a+\epsilon\Delta(\theta',t)} w(|\mathbf{r}-\mathbf{r}'|)(1-\bar{h}-\bar{f})r'dr'd\theta' - \frac{1}{\epsilon}\bar{u}. \tag{30}$$

To obtain an equation describing the dynamics for Φ, we differentiate Eq. (28) to get

$$\partial_t \Phi(\mathbf{r},t) = \int_0^{2\pi}\int_0^{a+\epsilon\Delta(\theta',t)} w(|\mathbf{r}-\mathbf{r}'|)\partial_t\varphi(\mathbf{r}',t)r'dr'd\theta' + \epsilon a\int_0^{2\pi} w(|\mathbf{r}-\mathbf{a}'|)\varphi(\mathbf{a}',t)\dot{\Delta}d\theta', \tag{31}$$

where $\mathbf{a}' = (a,\theta')$. We then substitute Eq. (23) into Eq. (31) to get

$$\partial_t \Phi(\mathbf{r},t) = -2\Phi - \Psi + \frac{1}{\epsilon}\int_0^{2\pi}\int_0^{a+\epsilon\Delta(\theta',t)} w(|\mathbf{r}-\mathbf{r}'|)(1-\bar{h}-2\bar{f})r'dr'd\theta' + \epsilon a\int_0^{2\pi} w(|\mathbf{r}-\mathbf{a}'|)\varphi(\mathbf{a}',t)\dot{\Delta}d\theta'. \tag{32}$$

Similarly,

$$\partial_t \Psi(\mathbf{r},t) = -p\Psi + \Phi + \epsilon a\int_0^{2\pi} w(|\mathbf{r}-\mathbf{a}'|)\psi(\mathbf{a}',t)\dot{\Delta}d\theta'. \tag{33}$$

The next step is to expand the integrals in Eq. (30) and Eq. (32) and then collect the terms of order ϵ^0. Together with Eq. (33), this gives a system of three equations that involves only μ, Φ, and Ψ. The expansions of these integrals are

$$\int_0^{2\pi}\int_0^{a+\epsilon\Delta(\theta',t)} w(|\mathbf{r}-\mathbf{r}'|)(1-\bar{h}-2\bar{f})r'dr'd\theta' = \epsilon a\int_{\mathcal{A}_+}\Delta(\theta',t)w(|\mathbf{r}-\mathbf{a}'|)d\theta', \tag{34}$$

and, similarly,

$$\int_0^{2\pi}\int_0^{a+\epsilon\Delta(\theta',t)} w(|\mathbf{r}-\mathbf{r}'|)(1-\bar{h}-\bar{f})r'dr'd\theta' = \bar{u} + \epsilon a\int_{\mathcal{A}_+}\Delta(\theta',t)w(|\mathbf{r}-\mathbf{a}'|)d\theta' + \epsilon a\frac{p}{1+2p}\int_{\mathcal{A}_-}\Delta(\theta',t)w(|\mathbf{r}-\mathbf{a}'|)d\theta', \tag{35}$$

where $\Delta(\theta,t)$ is given by Eq. (27) and $\mathcal{A}_\pm = \{\theta|\mu(a,\theta,t)\gtrless 0\}$ denotes the set of points on the bump boundary with positive or negative perturbations, respectively. Note that we have used the property $1-\bar{h}-2\bar{f}=0$ and $1-\bar{h}-\bar{f}=\bar{f}$ for $r<a$ to simplify the integral over the integration range $r\in[0,a)$. Combining these results and collecting terms of order ϵ^0, we have

$$\begin{cases} \dfrac{\partial\mu}{\partial t} = -\mu(\mathbf{r},t) - \Phi(\mathbf{r},t) - \Psi(\mathbf{r},t) + \mathcal{I}_+(\mathbf{r},t) + \dfrac{p}{1+2p}\mathcal{I}_-(\mathbf{r},t), \\ \dfrac{\partial\Phi}{\partial t} = -2\Phi(\mathbf{r},t) - \Psi(\mathbf{r},t) + \mathcal{I}_+(\mathbf{r},t), \\ \dfrac{\partial\Psi}{\partial t} = -p\Psi(\mathbf{r},t) + \Phi(\mathbf{r},t), \end{cases} \tag{36}$$

where

$$\mathcal{I}_\pm(\mathbf{r},t) = \frac{a}{|\bar{u}'(a)|}\int_{\mathcal{A}_\pm}\mu(a,\theta',t)w(|\mathbf{r}-\mathbf{a}'|)d\theta'. \tag{37}$$

The bump stability can therefore be obtained by analyzing the linear stability of Eq. (36). To proceed with the analysis, we have to restrict ourselves to the case where perturbations do not change the sign over time, that is, $\mathcal{A}_\pm$ is constant over time. Under this condition, we can express a general perturbation in the form $\mu(\mathbf{r},t) = e^{\lambda t}\mu(\mathbf{r})$, $\Phi(\mathbf{r},t) = e^{\lambda t}\Phi(\mathbf{r})$, and $\Psi(\mathbf{r},t) = e^{\lambda t}\Psi(\mathbf{r})$, with λ being real valued. If we substitute them into Eq. (36), we obtain the following "eigenvalue" problem,

$$\begin{bmatrix} \lambda+1 & 1 & 1 \\ 0 & \lambda+2 & 1 \\ 0 & -1 & \lambda+p \end{bmatrix}\begin{bmatrix} \mu(\mathbf{r}) \\ \Phi(\mathbf{r}) \\ \Psi(\mathbf{r}) \end{bmatrix} = \begin{bmatrix} \mathcal{I}_+ + \frac{p}{1+2p}\mathcal{I}_- \\ \mathcal{I}_+ \\ 0 \end{bmatrix}. \tag{38}$$

The matrix on the left-hand side is not invertible if its determinant is zero; that is,

$$(\lambda+1)[\lambda^2 + (2+p)\lambda + 2p + 1] = 0. \tag{39}$$

Solutions to this equation are $\lambda = -1, \frac{1}{2}[-2-p\pm\sqrt{p(p-4)}]$, which have negative real parts for all $0\leqslant p\leqslant 1$, and they do not incur instability to the bump. In order to determine the bump stability, we now consider the case that the matrix in Eq. (38) is invertible. Solving Eq. (38) for $\mu(\mathbf{r})$ leads to

$$(\lambda+1)\mu(\mathbf{r}) = [1-k(\lambda)]\mathcal{I}_+ + \frac{p}{1+2p}\mathcal{I}_-, \tag{40}$$

where

$$k(\lambda) = \frac{\lambda+p+1}{\lambda^2+(2+p)\lambda+2p+1}. \tag{41}$$

Now consider the bump boundary by setting $r = a$. The spatial integrals are simplified to [41]

$$\mathcal{I}_{\pm}(a,\theta) = \frac{a}{|\bar{u}'(a)|}\int_{\mathcal{A}_{\pm}} \mu(a,\theta')w\left(2a\sin\frac{\theta-\theta'}{2}\right)d\theta'. \quad (42)$$

The stability of the bump depends on the sign of the perturbation $\Delta(\theta)$ to the bump boundary at $r = a$, which, in turn, depends on $\mu(a,\theta)$. There are three general cases to be considered, namely, a radially symmetric contraction, a radially symmetric expansion, and radially asymmetric perturbations to the bump boundary. The stabilities for radially symmetric perturbations, i.e., contraction and expansion, can be obtained analytically, whereas those for radially asymmetric ones require a numerical approximation scheme as in [41]. First, consider a radially symmetric contraction, with $\mu(a,\theta) = \mu(a) < 0$, $\mathcal{A}_+ = \varnothing$, and $\mathcal{A}_- = [0,2\pi)$. Under these conditions, Eq. (40) becomes

$$\lambda = -1 + \frac{p}{1+2p}\mathcal{J}(a), \quad (43)$$

with

$$\mathcal{J}(a) = \frac{2a}{|\bar{u}'(a)|}\int_0^{\pi} w(2a\sin\theta)d\theta. \quad (44)$$

For the coupling function used here, $\mathcal{J}(a)$ has an explicit analytical expression [41],

$$\mathcal{J}(a) = \frac{1+2p}{p}\frac{W_E\mathcal{J}_0(a,\sigma_E) - W_I\mathcal{J}_0(a,\sigma_I)}{W_E\mathcal{J}_1(a,\sigma_E) - W_I\mathcal{J}_1(a,\sigma_I)}, \quad (45)$$

with

$$\mathcal{J}_i(a,\sigma) = I_i(a/\sigma)K_i(a/\sigma) - I_i(2a/\sigma)K_i(2a/\sigma). \quad (46)$$

Next we consider a radially symmetric expansion, with $\mu(a,\theta) = \mu(a) > 0$, $\mathcal{A}_- = \varnothing$, and $\mathcal{A}_+ = [0,2\pi)$. Under these conditions, Eq. (40) becomes

$$\lambda + 1 = [1 - k(\lambda)]\mathcal{J}(a), \quad (47)$$

which gives a quadratic equation,

$$\lambda^2 + (2 + p - \mathcal{J})\lambda + 1 + 2p - \mathcal{J}p = 0. \quad (48)$$

The results for perturbations corresponding to radially symmetric contraction and expansion are shown in Fig. 3. The lower branch of Fig. 2, as shown in Fig. 3(a), has positive eigenvalues for both contraction (dashed) and expansion (solid) for all p values for which a bump exists. The upper branch of Fig. 2, as shown in Fig. 3(b), is stable with respect to contraction (dashed) for all p values, but unstable with respect to an expansion for $p < 0.129$. For $p > 0.129$, the analysis does not indicate the stability of an expansion, due to nonzero imaginary parts of the eigenvalues violating the assumption that the perturbations do not switch signs. Nonetheless, numerical simulation shows that the bump appears to be stable over this range.

Finally, we consider general cases with radially asymmetric perturbations with $\mathcal{A}_{\pm} \neq \varnothing$. There is no systematic way to obtain analytical solutions to the eigenvalue problem [Eq. (38)], which has to be solved numerically. Nonetheless, due to the translational invariance of the neural field, we expect

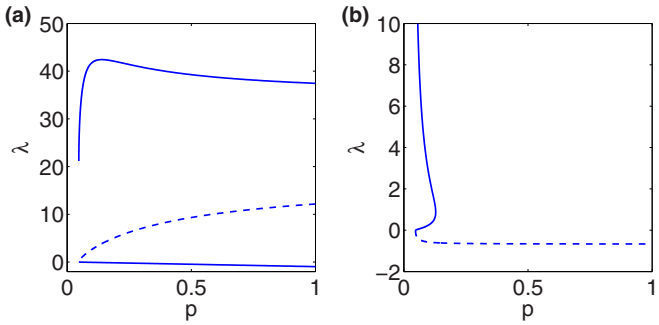

FIG. 3. (Color online) The eigenvalue λ of the linearized system with respect to radially symmetric perturbations. (a) A bump solution with a small radius is unstable ($\lambda > 0$) to both contraction (dashed) and expansion (solid) for all p values. (b) A bump solution with a large radius is stable to contraction (dashed) for all p, but it is unstable to expansion (solid) for $p < 0.129$. Stability about expansion for $p > 0.129$ cannot be inferred, but simulation nonetheless indicates that it is stable.

the existence of a zero eigenvalue for a shift perturbation, which can be verified analytically. Following the steps in [41], we set $\lambda = 0$ and $\mu(a,\theta) = e^{i\theta}$ in Eq. (40) and get

$$1 = \frac{p}{1+2p}\frac{2a}{|\bar{u}'(a)|}\int_0^{\pi} e^{2i\theta'}w(2a\sin\theta')d\theta'. \quad (49)$$

The integral on the right-hand side is real, since

$$\mathrm{Im}\left\{\int_0^{\pi} e^{2i\theta'}w(2a\sin\theta')d\theta'\right\} = \int_0^{\pi}\sin 2\theta' w(2a\sin\theta')d\theta' = 0, \quad (50)$$

due to the integrand being odd symmetric about $\pi/2$. For the Mexican hat coupling function used here, the real part of the integral can be expressed explicitly by using the identity $\int_0^{\pi} K_0(2a\sin\theta)\cos 2\theta d\theta = \pi I_1(a)K_1(a)$. Finally, by using

$$|\bar{u}'(a)| = \frac{4a}{3}\frac{p}{1+2p}[W_E\mathcal{J}_1(a,\sigma_E) - W_I\mathcal{J}_1(a,\sigma_I)], \quad (51)$$

we find that Eq. (49) is satisfied; that is, there exists an eigenvalue $\lambda = 0$.

To find other solutions to the eigenvalue problem [Eq. (38)], we apply the following numerical scheme [41]. Discretize the spatial coordinate as $\theta_j = 2\pi\frac{j}{N}$, $j = 0,1,\ldots,N-1$, and consider perturbations such that $\mathcal{A}_{\pm}$ is the union of $n \geqslant 1$ disconnected, evenly distributed, and equally sized subregions with $\mu(a,\theta_i) \gtrless 0$. To fully characterize the set of possible eigenmodes for each n, the size l of each subregion of $\mathcal{A}_+$ is taken to be anywhere from 1 to $N/n - 1$. For a radially symmetric perturbation, denoted $n = 0$, we have $l = 0$ for a contraction and $l = N$ for an expansion. Let

$$w_{jk} = w\left(2a\sin\frac{\theta_j - \theta_k}{2}\right) \quad (52)$$

and approximate the integral of Eq. (42) using

$$\mathcal{I}_{\pm}(a,\theta_j) \approx \frac{a}{|\bar{u}'(a)|}\frac{2\pi}{N}\sum_{\mathcal{A}_{\pm}}\mu(a,\theta_k)w_{jk}. \quad (53)$$

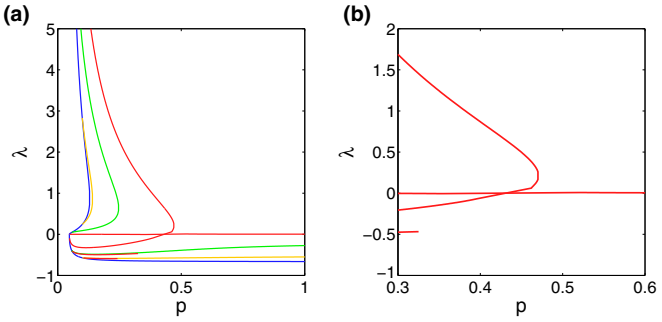

FIG. 4. (Color online) The eigenvalue λ of the linearized system with respect to radially asymmetric perturbations. (a) Eigenvalues of different modes of perturbations with order $n = 0,1,2,3$, colored in blue, red, green, and yellow, respectively (with increasing brightness). The dominant mode has order $n = 1$ (red), corresponding to a shift perturbation. The shift perturbation has a zero eigenvalue, as expected from the translational invariance of the system; for $p \leqslant 0.470$, positive eigenvalues emerge, indicating that the shift perturbation is unstable. A number of $N = 120$ points is used to discretize the angular coordinate θ. (b) Magnification of the eigenvalue for shift perturbation ($n = 1$) near the critical point, with higher accuracy using $N = 480$ points for discretizing θ.

Applying this approximation to Eq. (38), we obtain a matrix eigenvalue problem, conveniently written in block matrix form,

$$\begin{bmatrix} W^+ + \frac{p}{1+2p}W^- - I & -I & -I \\ W^+ & -2I & -I \\ 0 & I & -pI \end{bmatrix} \begin{bmatrix} \mu(\mathbf{r}) \\ \Phi(\mathbf{r}) \\ \Psi(\mathbf{r}) \end{bmatrix} = \lambda \begin{bmatrix} \mu(\mathbf{r}) \\ \Phi(\mathbf{r}) \\ \Psi(\mathbf{r}) \end{bmatrix}, \tag{54}$$

where I is the N-by-N identity matrix. The matrix $W^{\pm}$ is an N-by-N matrix whose entries are given by

$$W^{\pm}_{jk} = \frac{a}{|\bar{u}'(a)|}\frac{2\pi}{N} w_{jk} \mathbf{1}^{\pm}_k, \tag{55}$$

where the indicator function $\mathbf{1}^{\pm}_k$ is equal to 1 if $\theta_k \in \mathcal{A}_{\pm}$ and 0 otherwise, and $|\bar{u}'(a)|$ is given by Eq. (51). For each mode n, we solve the eigenvalue problem of Eq. (54) numerically for every l and find the corresponding eigenfunctions $\mu(a,\theta)$. A valid solution to the eigenfunction is found if either $\mu(a,\theta)$ or $-\mu(a,\theta)$ satisfies the initial assumption about the signs of the perturbations. It turns out for each n, only one or two valid solutions are found for a given p value.

Since we have shown analytically that the lower branch in Fig. 2 is always unstable for perturbations of order $n = 0$, we now focus on the upper branch. We calculate the eigenvalues for modes $n = 0,1,2,3$ for the upper branch in Fig. 2, which are shown in Fig. 4. Note that only those eigenvalues that are real valued are shown. The dominant order corresponds to a shift perturbation, shown in red. It contains a zero eigenvalue due to the translational invariance of the system. However, an asymmetric shift perturbation incurs instability below a critical point, $p = 0.47$, which approximately coincides with the point of symmetry breaking, $p = 0.49$, found by direct numerical simulations. Our analysis suggests that the transition from radially symmetric bumps to localized propagating waves is due to this shift instability. The result of our analysis is also consistent with the critical point for symmetry breaking found in the spiking network model [13,45], from which this neural field is derived. The spatial eigenmodes are characterized by the fractions of the bump boundary with positive perturbations, $|\mathcal{A}_+|$, as shown in Fig. 5(a). Examples of stable and unstable eigenmodes for $n = 1,2,3$ are shown in Figs. 5(b)–5(d).

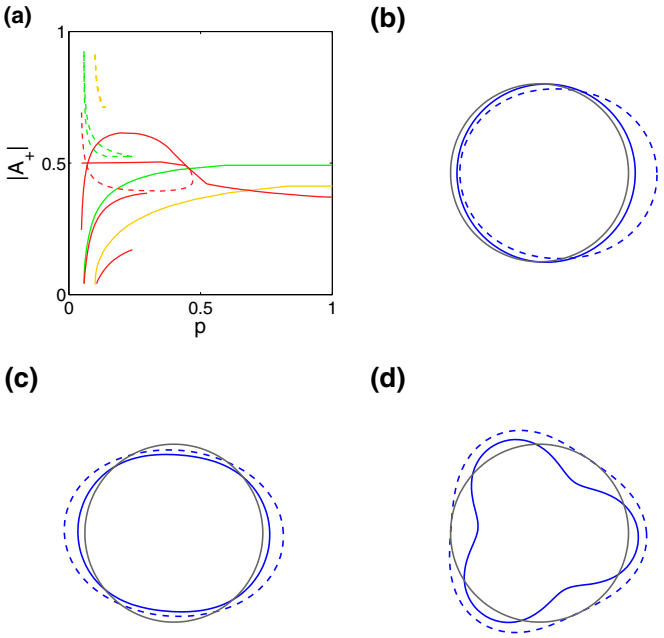

FIG. 5. (Color online) Shapes of eigenmode perturbations. (a) The fraction of the region over which the eigenmode perturbation is positive along the bump boundary. Spatial modes $n = 1,2,3$ are colored in red, green, and yellow, respectively (with increasing brightness). Solid (dashed) curves corresponds to stable (unstable) modes. (b)–(d) Examples of stable (solid) and unstable (dashed) eigenmodes for $n = 1,2,3$. The gray circle represents the boundary of the unperturbed bump.

V. PROPAGATING WAVE

Localized propagating waves that emerge from our neural-field model can be characterized by a homoclinic orbit by considering the system in a comoving frame. Letting $\xi = x/c - t$, where c is the wave speed, a steady-state solution $[F(\xi,y), H(\xi,y)]$ of the wave in the comoving frame satisfies

$$\begin{cases} -\partial_\xi F = -F + (1 - H - F)\phi(cw * F), \\ -\partial_\xi H = -pH + F, \end{cases} \tag{56}$$

where $w * F$ is a spatial convolution with respect to (ξ,y). When $\phi(u) = H(u - \kappa)$, we expect a solution such that $U = cw * F > \kappa$ for a region A_+ and $U < \kappa$ for a region A_-. For the region A_+, the equations for the steady state reduces to

$$\begin{cases} -\partial_\xi F = -2F - H + 1, \\ -\partial_\xi H = -pH + F. \end{cases} \tag{57}$$

This set of equations has an unstable focus at $(\bar{F},\bar{H}) = (\frac{p}{1+2p}, \frac{1}{1+2p})$. For the region A_-, the equations for the steady

state are

$$\begin{cases} -\partial_\xi F = -F, \\ -\partial_\xi H = -pH + F, \end{cases} \tag{58}$$

which have an unstable node at $(\bar{F},\bar{H}) = (0,0)$. Suppose that the A_+ is a simply connected region defined by the set $A_+ = \{(\xi,y)|\sigma_-(y) < \xi < \sigma_+(y), y \in [-b,b]\}$. By imposing a continuous boundary condition, such that $F(\sigma_+(y),y) = 0$ and $\lim_{\xi\to\sigma_-(y)^+} F(\xi,y) = \lim_{\xi\to\sigma_-(y)^-} F(\xi,y)$, we can solve the linear equations given by Eqs. (57) and (58) and construct a homoclinic orbit. The solution is

$$F(\xi,y) = \begin{cases} 0, & \text{for} \quad \xi > \sigma_+(y), \\ \frac{p}{1+2p}\{1 - e^{\alpha(\xi-\sigma_+)}[\cos\beta(\xi-\sigma_+) + A\sin\beta(\xi-\sigma_+)]\}, & \text{for} \quad \sigma_-(y) \leqslant \xi \leqslant \sigma_+(y), \\ F_-(y)e^{\xi-\sigma_-}, & \text{for} \quad \xi < \sigma_-(y), \end{cases} \tag{59}$$

where $\alpha = (2+p)/2$, $\beta = \sqrt{p(4-p)}/2$, $F_\pm(y) = F(\sigma_\pm(y),y)$, and $A = \frac{2-a+1/p}{\beta}$, and

$$H(\xi,y) = \begin{cases} 0, & \text{for} \quad \xi > \sigma_+(y), \\ \frac{1}{1+2p}\{1 - e^{\alpha(\xi-\sigma_+)}[\cos\beta(\xi-\sigma_+) + B\sin\beta(\xi-\sigma_+)]\}, & \text{for} \quad \sigma_- \leqslant \xi \leqslant \sigma_+, \\ \left[H_-(y) + \frac{F_-(y)}{1-p}\right]e^{p(\xi-\sigma_-)} - \frac{F_-(y)}{1-p}e^{\xi-\sigma_-}, & \text{for} \quad \xi < \sigma_-(y), \end{cases} \tag{60}$$

where $B = \frac{a-2-p[(\alpha-2)^2+\beta^2]}{\beta}$. The boundary of the excited region A_+ satisfies the threshold condition $u(\xi,y) = \kappa$,

$$\kappa = c\int_{-b}^{b}\int_{-\infty}^{\sigma_+(y')} w(|\mathbf{a}-\mathbf{r}'|)F(\xi',y')d\xi' dy', \tag{61}$$

where $\mathbf{a} = (c\sigma_\pm(y),y)$ and $\mathbf{r}' = (c\xi',y')$. There is no simple way to analytically solve the above equation and to determine the boundary or the wave speed. Nonetheless, by using the boundary obtained from simulation, we can then determine the homoclinic orbit described by Eqs. (59) and (60).

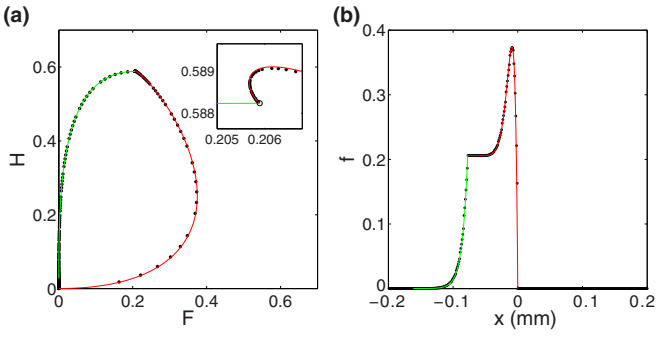

FIG. 6. (Color online) Spatial profile of propagating waves. (a) Longitudinal profile of a wave corresponds to a piecewise smooth homoclinic orbit on the F-H plane at $p = 0.35$. The sections of the orbit corresponding to the front and the tail of the wave are shown in red (darker shade) and green (lighter shade), respectively. For the red section, the synaptic input satisfies $u > \kappa$, and the orbit spirals from the origin towards the unstable focus at $(F,H) = (\frac{p}{1+2p}, \frac{1}{1+2p})$ in the $-\xi$ direction. For the green section, $u < \kappa$, and the orbit decays exponentially towards the origin in the $-\xi$ direction. (Inset) Magnification near the unstable focus (marked with a circle). Note that the orbit does not connect the circle, but has a sharp bend at the boundary specified by $u = \kappa$. (b) Longitudinal section of a wave propagating to the right, with a numerically measured speed of $c = 84.2$ mm/s at $p = 0.35$. The wave profile obtained from the simulation (dots) is in agreement with the analytical solution (solid curve).

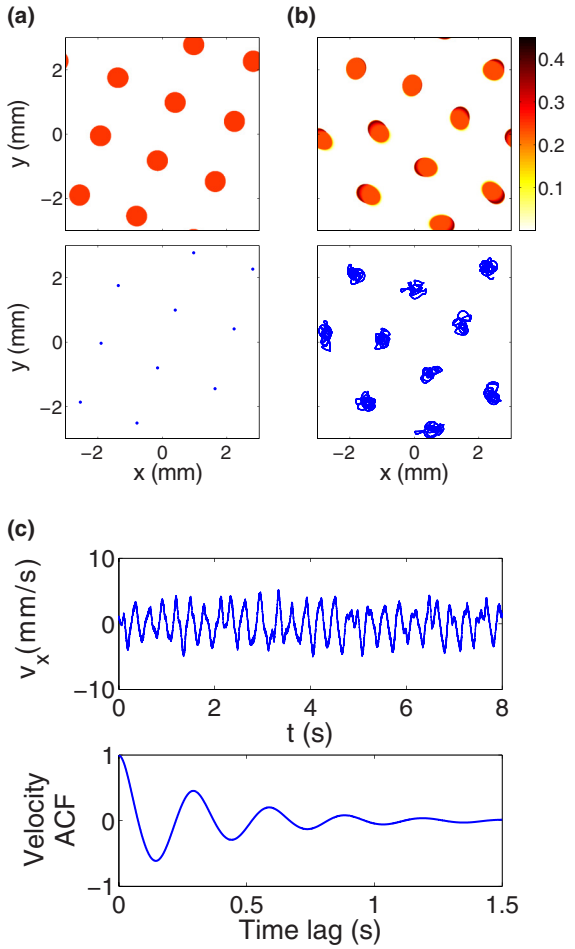

FIG. 7. (Color online) Dynamics of multiple localized patterns. (a) Snapshots of $f(\mathbf{r},t)$ with $N = 10$ stationary bumps at $p = 0.49$ arranged on a square lattice (top) and their corresponding trajectories (bottom). (b) Rotating waves with irregular interactions at $p = 0.44$. (c) The velocity time series of a rotating wave (top) and its ACF (bottom). The ACF shows a sinusoidal oscillation with an exponentially decaying envelope.

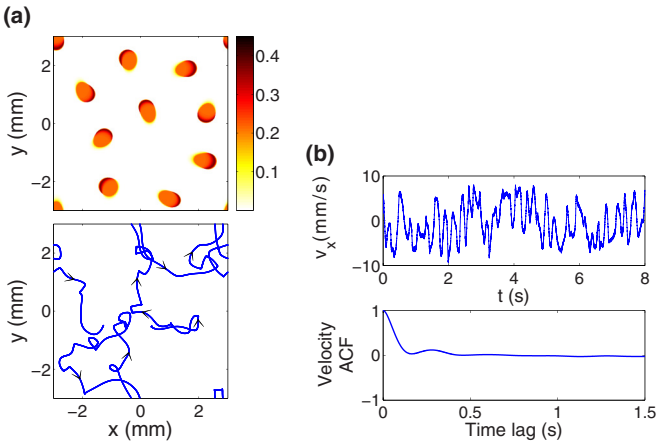

FIG. 8. (Color online) Multiple waves with complex interactions. (a) Snapshot of $f(\mathbf{r},t)$ with $N = 10$ waves with complex interactions at $p = 0.38$ (top) and the irregular trajectory of one of the waves (bottom). The arrows indicate the propagation direction of the waves. (b) The velocity of the waves with complex interaction (top) and the corresponding ACF (bottom).

Figure 6(a) shows the homoclinic orbit corresponding to the longitudinal profile of the wave through its central axis ($y = 0$), with refractoriness parameter $p = 0.35$. The red curve corresponds to the front of the wave, where $\sigma_-(0) < \xi < \sigma_+(0) = 0$, and the green curve corresponds to the tail of the wave, where $\xi < \sigma_-(0)$. The inset in Fig. 6(a) is a magnification showing the shape of the orbit near the unstable focus of Eq. (57) (marked with a circle). Note that the red curve intersects with the green curve without connecting the unstable focus. By using the wave speed c measured from the simulation, we can also determine the longitudinal profile of the wave, as shown in Fig. 6(b). The profile derived analytically (solid line) is in agreement with the simulation result (dots). The derivation above can be naturally extended to a rotating wave by considering the neural field in a rotating polar coordinate, $F(r,\xi)$, where $\xi = \theta/\omega - t$ and ω is the angular speed.

VI. COLLECTIVE DYNAMICS OF MULTIPLE LOCALIZED PROPAGATING WAVES

Having analyzed the dynamics of a single localized pattern, we now consider the collective dynamics of multiple such

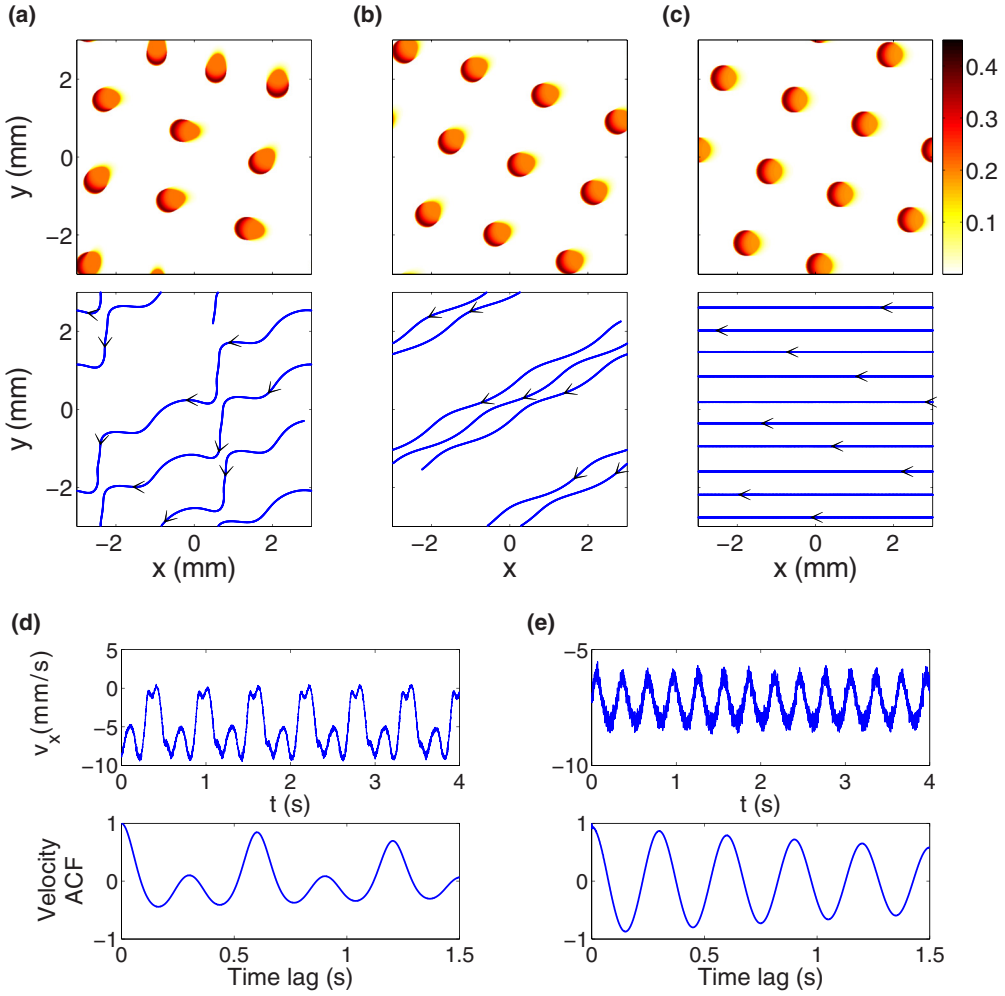

FIG. 9. (Color online) Regularly propagating waves. (a),(b) Snapshots of $f(\mathbf{r},t)$ of $N = 10$ propagating waves (top) and their trajectories (bottom) at $p = 0.35$ and $p = 0.33$, respectively. The propagation involves a net drift in a fixed direction, superimposed by period-2 (a) and period-1 (b) oscillations. For clarity, the trajectory of only one of the waves is shown for each case. (c) For $p = 0.3$, the waves traveling uniformly in a fixed direction. (d),(e) Velocity and the corresponding ACF for $p = 0.35$ and $p = 0.33$, respectively.

patterns, which can be evoked when transient external inputs are added to different locations of the neural-field model. We simulate multiple patterns on a 6 × 6-mm square domain with periodic boundary conditions. When these patterns are close to each other, they have repulsive interactions due to the lateral inhibition [Eq. (12)]. For $p > 0.48$, multiple stationary bumps can be generated, and they eventually arrange themselves to a square lattice, as shown in Fig. 7(a). As p decreases, the bump destabilizes and evolves to localized propagating waves as $p \leqslant 0.48$. As demonstrated above, depending on the value of p, a single wave can move along a circle or a straight line. However, complex dynamics occurs for multiple waves due to their repulsive interactions. For $0.42 < p \leqslant 0.48$, each wave tends to rotate around a confined area, as expected from a single, isolated rotating wave, but with visible irregularity due to interactions with other waves; as shown in Fig. 7(b), their trajectories no longer follow perfect circular paths as an isolated rotating wave in Fig. 1(b). To characterize the irregular interactions, we trace the individual trajectories of the waves and calculate the autocorrelation functions (ACFs) of their velocities. Figure 7(c) shows the velocity along the x axis of one of the multiple rotating waves at $p = 0.44$ and its ACF (bottom panel). The velocity ACF shows a sinusoidal oscillation with an exponentially decaying envelope, with a decay constant $\tau \approx 0.382$ s. This indicates that the multiple rotating waves have periodic oscillations embedded with irregular fluctuations due to interactions with other waves.

For $0.36 < p \leqslant 0.42$, each crescent-shaped wave tends to move in a straight line by itself, but change direction upon colliding with other waves, resulting in complex and irregular trajectories, as shown in Fig. 8(a). For $p = 0.38$, the velocity ACF decays towards zero as the time lag increases, consistent with the irregular motion of the waves. The velocity ACF is also strictly positive, consistent with that the waves move in straight lines and change directions only if they collide with each other. Interestingly, the ACF does not decay monotonically, but it has a local minimum at $\Delta t \approx 0.165$ s and a peak at $\Delta t \approx 0.28$ s. The velocity of the wave is the least correlated with itself at the time lag corresponding to this local minimum. To understand this point, we calculate the average intercollision interval of individual waves; a collision is considered to occur when the distance between two waves becomes less than a threshold $r = 1.65$ mm. We find that the average intercollision interval of each wave is approximately $\Delta t = 0.16$ s. This therefore indicates that the extrema in the velocity ACF approximately corresponds to the average intercollision interval.

As p further decreases, however, the motion of the waves converges towards the same direction. Closer inspection reveals periodic oscillations in the trajectory of each wave, superimposed on a uniform linear motion. These periodic oscillations are originated from the periodic collisions between the waves. Snapshots of these uniformly traveling waves with periodic collisions at $p = 0.35$ and $p = 0.33$ and their corresponding trajectories are shown in Figs. 9(a) and 9(b), where small amplitude oscillations are clearly visible. For both $p = 0.35$ and $p = 0.33$, the velocity shows periodic oscillations around a constant value [see Figs. 9(d) and 9(e)]. For $p = 0.33$, the velocity ACF shows sinusoidal oscillations

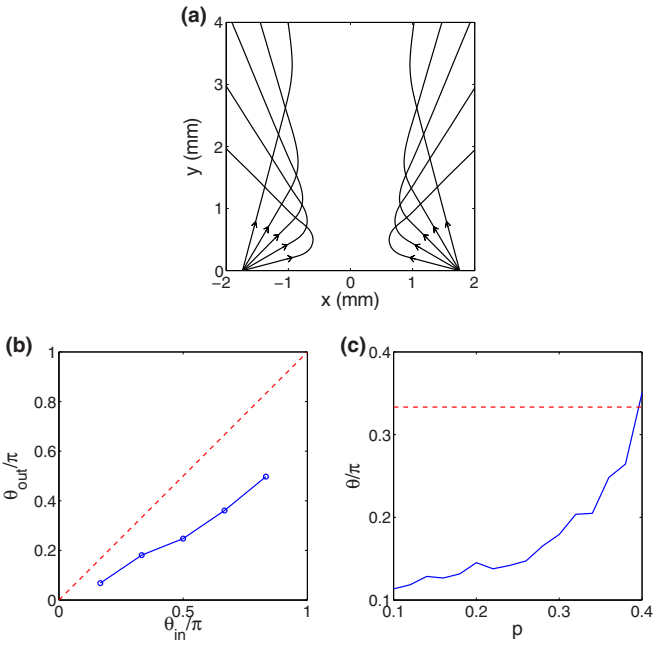

FIG. 10. (Color online) Inelastic repulsive collision of two waves. (a) Trajectories of two waves colliding with various angles at $p = 0.3$. (b) Outgoing angle versus incoming angle. The outgoing angle is smaller than the incoming angle, indicating that the collision is inelastic. (c) Outgoing angle versus p. The outgoing angle of the collision decreases as p decreases, indicating that the collision is more inelastic for smaller p. The dashed lines indicate the incoming angle.

with a decaying envelope, indicating a period-1 oscillation, whereas for $p = 0.35$, the ACF shows oscillations with alternating amplitudes, indicating a period-2 oscillation. This doubling of the period in the trajectory reflects the change in the collision patterns of the waves. For $p \leqslant 0.3$, the waves converge towards a motion in a straight line [Fig. 9(c)], the same as a single isolated wave in this parameter range.

To illustrate the repulsive interactions of the localized propagating waves, we trace the trajectories of two waves colliding symmetrically at different angles [Fig. 10(a)]. It is found that the outgoing angle of the collision is less than the incoming angle, suggesting that the collision is inelastic [Fig. 10(b)]. Interestingly, for a collision with a fixed incoming angle, its outgoing angle becomes smaller as p decreases, suggesting that refractoriness contributes to strong inelastic collisions [Fig. 10(c)]. We also consider a special case of a perfectly aligned, head-on collision between two identical waves. Under this scenario, the waves may either bounce straight back to the opposite direction or merge with each other depending on the refractory parameter p. A series of snapshots of the temporal process of the head-on collision under each of these conditions is shown in Fig. 11. For $p = 0.1$, the waves physically touch each other and merge to a single transient bump. This bump is unstable, as expected by our stability analysis from previous sections, and it splits into two localized waves propagating in directions perpendicular to that of the incoming waves. For $p = 0.2$, corresponding to a relatively shorter refractory period, the waves do not

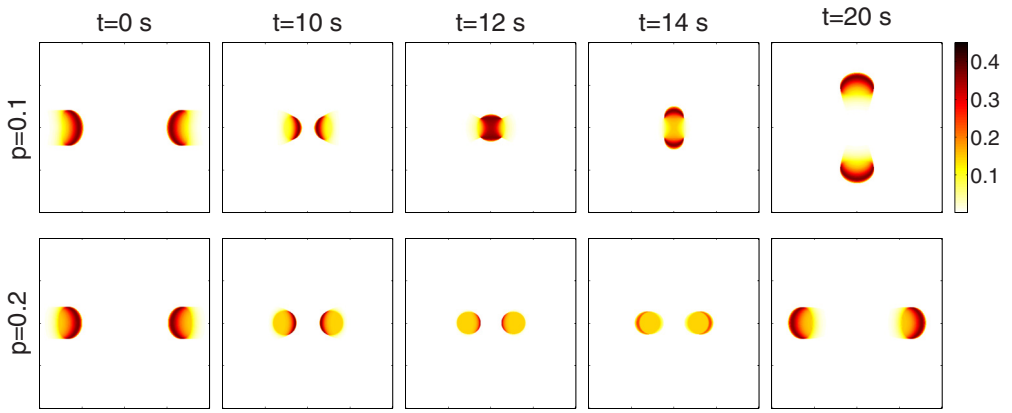

FIG. 11. (Color online) Head-on collisions between two waves. Snapshots of $f(\mathbf{r},t)$ of two localized propagating waves undergoing perfectly aligned head-on collision. At $p = 0.1$, the waves collide and merge with each other to form a single transient bump, which then splits into two waves along the direction perpendicular to the incoming waves. At $p = 0.2$, the waves collide and bounce straight back in the opposite directions.

touch each other, but bounce straight back to the opposite directions. These results show that refractoriness alone can influence the outcome of the head-on collision between two waves without changing the range or the strength of the lateral inhibition.

VII. CONCLUSION AND DISCUSSION

In this study, we have derived a two-dimensional neural field with nonlinear negative feedback in the form of refractoriness; the neural field is able to generate a range of localized patterns including stationary bumps and localized rotating and propagating waves. We have found refractoriness-induced symmetry breaking of stationary bumps into crescent-shaped propagating waves. To understand the mechanism underlying this symmetry breaking, we have constructed explicit bump solutions to the neural field and analyzed their linear stability under different eigenmode perturbations. The analysis shows that the symmetry breaking occurs through the instability of an asymmetric shift perturbation. When multiple localized waves are present, the two-dimensional neural-field model generates rich collective dynamics, including periodic and irregular interactions between them.

Refractoriness has appeared in the neural-field model originally proposed by Wilson and Cowan [38], but very few studies have investigated its effect on the dynamics of spatially extended neural fields. Very recently, the generation of spatiotemporally periodic pulses through Turing instability has been analyzed in a one-dimensional neural field with refractoriness [30]. To the best of our knowledge, the analysis in the present paper is the first to investigate refractoriness-induced symmetry breaking of two-dimensional bumps in a neural field. We find that refractoriness induces a shift instability that causes a radially symmetric bump to evolve into a localized propagating wave in response to small perturbations. The refractoriness happens immediately after a spike and its period ranges from 1 to 8 ms [20]; thus, it occurs faster as compared with spike frequency adaptation or synaptic depression considered in other neural-field models [39–41]. Given that refractoriness is a fundamental biophysical feature common to all neurons in the brain, one would expect that refractoriness-induced symmetry breaking might be widely applicable in understanding the formation of traveling waves in neural systems.

Neural fields with two spatial dimensions exhibit a range of dynamic patterns, including spiral waves and target waves, and localized propagating waves. Localized propagating waves formed in two-dimensional spiking neural networks have been recently studied as a mechanism for generating spike sequences [46–49] and for accounting for variability in neural dynamics [50]. Our present study may provide theoretical insight into understanding the dynamics of these models. Our neural-field model also generates multiple localized waves with rich collective dynamics due to their interactions. Depending on the strength of the refractoriness, such wave patterns can move along linear trajectories, period-1 or period-2 oscillating trajectories, or irregular trajectories. The dynamics of these waves with complex interactions exhibit nontrivial correlations. Our results of multiple waves with complex interactions thus advances the existing studies of neural fields that have mainly focused on a single wave or multiple waves with regular dynamics [30,40,41]. As recently proposed in [12], multiple localized propagating patterns appear to be well suited for performing distributed dynamic computation in neural systems. The analytical tractability of our neural-field model and the complex wave dynamics emerging from it could potentially provide further insights into understanding the computational roles of multiple interacting waves in the future.

[1] V. K. Vanag and I. R. Epstein, Chaos **17**, 037110 (2007).
[2] N. Akhmediev and A. Ankiewicz, *Dissipative Solitons: From Optics to Biology and Medicine* (Springer, Berlin, 2005).
[3] M. Bär, M. Eiswirth, H.-H. Rotermund, and G. Ertl, Phys. Rev. Lett. **69**, 945 (1992).
[4] Y. A. Astrov and Y. A. Logvin, Phys. Rev. Lett. **79**, 2983 (1997).

[5] Y. A. Astrov, E. Ammelt, and H. G. Purwins, Phys. Rev. Lett. **78**, 3129 (1997).
[6] D. Peak, J. D. West, S. M. Messinger, and K. A. Mott, Proc. Natl. Acad. Sci. USA **101**, 918 (2004).
[7] U. Euteneuer and M. Schliwa, Nature (London) **310**, 58 (1984).
[8] T. D. Pollard, Nature (London) **422**, 741 (2003).
[9] D. G. Míguez, V. K. Vanag, and I. R. Epstein, Proc. Natl. Acad. Sci. USA **104**, 6992 (2007).
[10] F. Han, N. Caporale, and Y. Dan, Neuron **60**, 321 (2008).
[11] T. Kenet, D. Bibitchkov, M. Tsodyks, A. Grinvald, and A. Arieli, Nature (London) **425**, 954 (2003).
[12] P. Gong and C. van Leeuwen, PLoS Comput. Biol. **5**, e1000611 (2009).
[13] P. Gong and P. A. Robinson, Phys. Rev. E **85**, 055101(R) (2012).
[14] N. Wiener and A. Rosenblueth, Arch. Inst. Cardiol. Mex. **16**, 205 (1946).
[15] J. Greenberg and S. Hastings, SIAM J. Appl. Math. **34**, 515 (1978).
[16] X. Cui, R. J. Rovetti, L. Yang, A. Garfinkel, J. N. Weiss, and Z. Qu, Phys. Rev. Lett. **103**, 044102 (2009).
[17] M. Gerhardt, H. Schuster, and J. Tyson, Science **247**, 1563 (1990).
[18] M. A. Buice and J. D. Cowan, Phys. Rev. E **75**, 051919 (2007).
[19] A. L. Hodgkin and A. F. Huxley, J. Physiol. **117**, 500 (1952).
[20] E. Kandel, J. Schwartz, T. Jessell, S. Siegelbaum, and A. Hudspeth, *Principles of Neural Science*, 5th ed. (McGraw-Hill, New York, 2012).
[21] M. J. Berry II and M. Meister, J. Neurosci. **18**, 2200 (1998).
[22] M. C. Teich, L. Matin, and B. I. Cantor, J. Opt. Soc. Am. **68**, 386 (1978).
[23] C. Koch, *Biophysics of Computation: Information Processing in Single Neurons* (Oxford University Press, New York, 1999).
[24] D. Hampel and P. Lansky, J. Neurosci. Methods **171**, 288 (2008).
[25] R. Curtu and B. Ermentrout, J. Math. Biol. **43**, 81 (2001).
[26] P. H. Chu, J. G. Milton, and J. D. Cowan, Int. J. Bifurcation Chaos **04**, 237 (1994).
[27] C. Fohlmeister, W. Gerstner, R. Ritz, and J. L. van Hemmen, Neural Comput. **7**, 905 (1995).
[28] B. Lindner, J. García-Ojalvo, A. Neiman, and L. Schimansky-Geier, Phys. Rep. **392**, 321 (2004).
[29] P. Jung and G. Mayer-Kress, Chaos **5**, 458 (1995).
[30] H. G. E. Meijer and S. Coombes, J. Math. Biol. **68**, 1249 (2014).
[31] Y. Lu, Y. Sato, and S. Amari, Neural Comput. **23**, 1248 (2011).
[32] M. Owen, C. Laing, and S. Coombes, New J. Phys. **9**, 378 (2007).
[33] S. E. Folias and P. C. Bressloff, Phys. Rev. Lett. **95**, 208107 (2005).
[34] M. Tsodyks, T. Kenet, A. Grinvald, and A. Arieli, Science **286**, 1943 (1999).
[35] D. Pinto and G. Ermentrout, SIAM J. Appl. Math. **62**, 206 (2001).
[36] S. Folias and P. Bressloff, SIAM J. Appl. Dyn. Syst. **3**, 378 (2004).
[37] S. Coombes, H. Schmidt, and I. Bojak, J. Math. Neurosci. **2**, 9 (2012).
[38] H. R. Wilson and J. D. Cowan, J. Biophys. **12**, 1 (1972).
[39] Z. P. Kilpatrick and P. C. Bressloff, Phys. D (Amsterdam, Neth.) **239**, 1048 (2010).
[40] Z. Kilpatrick and P. Bressloff, J. Comput. Neurosci. **28**, 193 (2010).
[41] P. C. Bressloff and Z. P. Kilpatrick, SIAM J. Appl. Math. **71**, 379 (2011).
[42] S. Coombes, Biol. Cybern. **93**, 91 (2005).
[43] Z. P. Kilpatrick and P. C. Bressloff, Phys. D (Amsterdam, Neth.) **239**, 547 (2010).
[44] P. C. Bressloff and S. Coombes, Cognit. Comput. **5**, 281 (2013).
[45] Y. Qi, M. Breakspear, and P. Gong, Neural Comput. **27**, 255 (2015).
[46] V. Itskov, C. Curto, E. Pastalkova, and G. Buzsáki, J. Neurosci. **31**, 2828 (2011).
[47] A. H. Azizi, L. Wiskott, and S. Cheng, Front. Comput. Neurosci. **7**, 161 (2013).
[48] S. Romani and M. Tsodyks, Hippocampus **25**, 94 (2015).
[49] J. H. C. Palmer and P. Gong, Neural Comput. **25**, 2833 (2013).
[50] A. Keane and P. Gong, J. Neurosci. **35**, 1591 (2015).